Mon. Not. R. Astron. Soc. **381,** 702–712 (2007) doi:10.1111/j.1365-2966.2007.12202.x

Cosmological constraints from the 100-deg^2 weak-lensing survey*

Jonathan Benjamin,[1]† Catherine Heymans,[1,2] Elisabetta Semboloni,[2,3] Ludovic Van Waerbeke,[1] Henk Hoekstra,[4] Thomas Erben,[3] Michael D. Gladders,[5] Marco Hetterscheidt,[3] Yannick Mellier[2,3,6] and H. K. C. Yee[7]

[1] *University of British Columbia, 6224 Agricultural Road, Vancouver, BC, Canada V6T 1Z1*
[2] *Institut d'Astrophysique de Paris, UMR7095 CNRS, Université Pierre & Marie Curie – Paris, 98 bis bd Arago, 75014 Paris, France*
[3] *Argelander-Institut für Astronomie (AIfA), Universität Bonn, Auf dem Hügel 71, 53121 Bonn, Germany*
[4] *Department of Physics and Astronomy, University of Victoria, Victoria, BC, Canada V8P 5C2*
[5] *Department of Astronomy & Astrophysics, University of Chicago, Chicago, IL 60637, USA*
[6] *Observatoire de Paris, LERMA, 61, avenue de l'Observatoire, 75014 Paris, France*
[7] *Department of Astronomy & Astrophysics, University of Toronto, Toronto, ON, Canada M5S 3H4*

Accepted 2007 July 5. Received 2007 June 12; in original form 2007 March 21

ABSTRACT

We present a cosmic shear analysis of the 100-deg^2 weak-lensing survey, combining data from the CFHTLS-Wide, RCS, VIRMOS-DESCART and GaBoDS surveys. Spanning $\sim$100 deg^2, with a median source redshift $z \sim 0.78$, this combined survey allows us to place tight joint constraints on the matter density parameter $\Omega_{\rm m}$, and the amplitude of the matter power spectrum σ_8, finding $\sigma_8(\Omega_{\rm m}/0.24)^{0.59} = 0.84 \pm 0.05$. Tables of the measured shear correlation function and the calculated covariance matrix for each survey are included as supplementary material to the online version of this article.

The accuracy of our results is a marked improvement on previous work owing to three important differences in our analysis; we correctly account for sample variance errors by including a non-Gaussian contribution estimated from numerical simulations; we correct the measured shear for a calibration bias as estimated from simulated data; we model the redshift distribution, $n(z)$, of each survey from the largest deep photometric redshift catalogue currently available from the CFHTLS-Deep. This catalogue is randomly sampled to reproduce the magnitude distribution of each survey with the resulting survey-dependent $n(z)$ parametrized using two different models. While our results are consistent for the $n(z)$ models tested, we find that our cosmological parameter constraints depend weakly (at the 5 per cent level) on the inclusion or exclusion of galaxies with low-confidence photometric redshift estimates ($z > 1.5$). These high-redshift galaxies are relatively few in number but contribute a significant weak-lensing signal. It will therefore be important for future weak-lensing surveys to obtain near-infrared data to reliably determine the number of high-redshift galaxies in cosmic shear analyses.

Key words: gravitational lensing – cosmological parameters – cosmology: observations – large-scale structure of Universe.

1 INTRODUCTION

Weak gravitational lensing of distant galaxies by intervening matter provides a unique and unbiased tool to study the matter distribution of the Universe. A large-scale structure in the Universe induces a weak-lensing signal, known as cosmic shear. This signal provides a direct measure of the projected matter power spectrum over a redshift range determined by the lensed sources and over scales ranging from the linear to non-linear regime. The unambiguous interpretation of the weak-lensing signal makes it a powerful tool for measuring cosmological parameters which complement those from other probes such as, cosmic microwave background anisotropies (Spergel et al. 2006) and type Ia supernovae (Astier et al. 2006).

Cosmic shear has only recently become a viable tool for observational cosmology, with the first measurements reported

*Based on observations obtained at the Canada–France–Hawaii Telescope (CFHT) which is operated by the National Research Council of Canada (NRCC), the Institut des Sciences de l'Univers (INSU) of the Centre National de la Recherche Scientifique (CNRS) and the University of Hawaii (UH).
†E-mail: jonben@phas.ubc.ca

© 2007 The Authors. Journal compilation © 2007 RAS

simultaneously in 2000 (Bacon, Refregier & Ellis 2000; Kaiser, Wilson & Luppino 2000; Van Waerbeke et al. 2000; Wittman et al. 2000). The data these early studies utilized were not optimally suited for the extraction of a weak-lensing signal. Often having a poor trade-off between sky coverage and depth, and lacking photometry in more than one colour, the ability of these early surveys to constrain cosmology via weak lensing was limited, but impressive based on the data at hand. Since these early results several large dedicated surveys have detected weak lensing by large-scale structure, placing competitive constraints on cosmological parameters (Hoekstra, Yee & Gladders 2002b; Bacon et al. 2003; Brown et al. 2003; Hamana et al. 2003; Jarvis et al. 2003; Rhodes et al. 2004; Massey et al. 2005; Heymans et al. 2005; Van Waerbeke, Mellier & Hoekstra 2005; Hoekstra et al. 2006; Semboloni et al. 2006; Schrabback et al. 2007). With the recent first measurements of a changing lensing signal as a function of redshift (Bacon et al. 2005; Wittman 2005; Semboloni et al. 2006; Massey et al. 2007b), and the first weak-lensing constraints on dark energy (Hoekstra et al. 2006; Jarvis et al. 2006; Kitching et al. 2007; Schimd et al. 2007), the future of lensing is promising.

There are currently several 'next generation' surveys being conducted. Their goal is to provide multicolour data and excellent image quality, over a wide field of view. Such data will enable weak lensing to place tighter constraints on cosmology, breaking the degeneracy between the matter density parameter $\Omega_{\rm m}$ and the amplitude of the matter power spectrum σ_8 and allowing for competitive constraints on dark energy. In this paper, we present an analysis of the 100-deg² weak-lensing survey that combines data from four of the largest surveys analysed to date, including the wide component of the Canada–France–Hawaii Telescope Legacy Survey (CFHTLS-Wide, Hoekstra et al. 2006), the Garching–Bonn Deep Survey (GaBoDS, Hetterscheidt et al. 2007), the Red-Sequence Cluster Survey (RCS, Hoekstra et al. 2002b) and the VIRMOS-DESCART survey (VIRMOS, Van Waerbeke et al. 2005). These surveys have a combined sky coverage of 113 deg² (96.5 deg², after masking), making this study the largest of its kind.

Our goal in this paper is to provide the best estimates of cosmology currently attainable by weak lensing, through a homogeneous analysis of the major data sets available. Our analysis is distinguished from previous work in three important ways. For the first time we account for the effects of non-Gaussian contributions to the analytic estimate of the sample variance – sometimes referred to as cosmic variance – covariance matrix (Schneider et al. 2002), as described in Semboloni et al. (2007). Results from the Shear TEsting Programme (STEP; see Heymans et al. 2006a; Massey et al. 2007a) are used to correct for calibration error in our shear measurement methods, a marginalization over the uncertainty in this correction is performed. We use the largest deep photometric redshift catalogue currently available (Ilbert et al. 2006), which provides redshifts for ∼500 000 galaxies in the CFHTLS-Deep. Additionally, we properly account for sample variance in our calculation of the redshift distribution, an important source of error discussed in Van Waerbeke et al. (2006).

This paper is organized as follows. In Section 2, we give a short overview of cosmic shear theory, and outline the relevant statistics used in this work. We describe briefly each of the surveys used in this study in Section 3. We present the measured shear signal in Section 4. In Section 5, we present the derived redshift distributions for each survey. We present the results of the combined parameter estimation in Section 6, closing thoughts and future prospects are discussed in Section 7.

2 COSMIC SHEAR THEORY

We briefly describe here the notations and statistics used in our cosmic shear analysis. For detailed reviews of the weak-lensing theory, the reader is referred to Munshi et al. (2006), Bartelmann & Schneider (2001) and Schneider et al. (1998). The notations used in the latter are adopted here. The power spectrum of the projected density field (convergence κ) can be written as

$$P_\kappa(k) = \frac{9\,H_0^4\,\Omega_{\rm m}^2}{4c^4}\int_0^{w_{\rm H}} \frac{{\rm d}w}{a^2(w)}\,P_{\rm 3D}\left(\frac{k}{f_K(w)};w\right) \times\left[\int_w^{w_{\rm H}} {\rm d}w' n(w')\frac{f_K(w'-w)}{f_K(w')}\right]^2, \quad (1)$$

where H_0 is the Hubble constant, $f_K(w)$ is the comoving angular diameter distance out to a distance w ($w_{\rm H}$ is the comoving horizontal distance), $a(w)$ is the scalefactor, and $n[w(z)]$ is the redshift distribution of the sources (see Section 5). $P_{\rm 3D}$ is the 3D mass power spectrum computed from a non-linear estimation of the dark matter clustering (see e.g. Peacock & Dodds 1996; Smith et al. 2003), and k is the 2D wavevector perpendicular to the line of sight. $P_{\rm 3D}$ evolves with time, hence its dependence on the comoving radial coordinate w.

In this paper, we focus on the shear correlation function statistic ξ. For a galaxy pair separation θ, we define

$$\xi_+(\theta) = \langle\gamma_{\rm t}(r)\gamma_{\rm t}(r+\theta)\rangle + \langle\gamma_{\rm r}(r)\gamma_{\rm r}(r+\theta)\rangle.$$
$$\xi_-(\theta) = \langle\gamma_{\rm t}(r)\gamma_{\rm t}(r+\theta)\rangle - \langle\gamma_{\rm r}(r)\gamma_{\rm r}(r+\theta)\rangle, \quad (2)$$

where the shear $\gamma = (\gamma_{\rm t}, \gamma_{\rm r})$ is rotated into the local frame of the line joining the centres of each galaxy pair separated by θ. The tangential shear is $\gamma_{\rm t}$, while $\gamma_{\rm r}$ is the rotated shear (having an angle of $\pi/4$ to the tangential component). The shear correlation function ξ_+ is related to the convergence power spectrum through

$$\xi_+(\theta) = \frac{1}{2\pi}\int_0^\infty {\rm d}k\,k\,P_\kappa(k)J_0(k\theta), \quad (3)$$

where J_0 is the zeroth-order Bessel function of the first kind. A quantitative measurement of the lensing amplitude and the systematics is obtained by splitting the signal into its curl-free (E-mode) and curl (B-mode) components, respectively. This method has been advocated to help the measurement of the intrinsic alignment contamination in the weak-lensing signal (Crittenden et al. 2001, 2002), but it is also an efficient measure of the residual systematics from the point spread function (PSF) correction (Pen, Van Waerbeke & Mellier 2002).

The E and B modes derived from the shape of galaxies are unambiguously defined only for the so-called aperture mass variance $\langle M_{\rm ap}^2\rangle$, which is a weighted shear variance within a cell of radius $\theta_{\rm c}$. The cell itself is defined as a compensated filter (Schneider et al. 1998), such that a constant convergence κ gives $M_{\rm ap} = 0$. $\langle M_{\rm ap}^2\rangle$ can be rewritten as a function of the tangential shear $\gamma_{\rm t}$ if we express $\gamma = (\gamma_{\rm t}, \gamma_{\rm r})$ in the local frame of the line connecting the aperture centre to the galaxy. $\langle M_{\rm ap}^2\rangle$ is given by

$$\left\langle M_{\rm ap}^2\right\rangle = \frac{288}{\pi\theta_{\rm c}^4}\int_0^\infty \frac{{\rm d}k}{k^3}P_\kappa(k)[J_4(k\theta_{\rm c})]^2. \quad (4)$$

The B-mode $\langle M_{\rm ap}^2\rangle_\perp$ is obtained by replacing $\gamma_{\rm t}$ with $\gamma_{\rm r}$. The aperture mass is insensitive to the mass sheet degeneracy, and therefore it provides an unambiguous splitting of the E and B modes. The drawback is that aperture mass is a much better estimate of the small-scale power than the large-scale power which can be seen from the function $J_4(k\theta_{\rm c})$ in equation (4) which peaks at $k\theta_{\rm c} \sim 5$.

© 2007 The Authors. Journal compilation © 2007 RAS, MNRAS **381,** 702–712

Essentially, all scales larger than a fifth of the largest survey scale remain inaccessible to $M_{\rm ap}$. The large-scale part of the lensing signal is lost by $M_{\rm ap}$, while the remaining small-scale fraction is difficult to interpret because the strongly non-linear power is difficult to predict accurately (Van Waerbeke et al. 2002). It is therefore preferable to decompose the shear correlation function into its E and B modes, as it is a much deeper probe of the linear regime.

Following Crittenden et al. (2001, 2002), we define

$$\xi'(\theta) = \xi_-(\theta) + 4\int_\theta^\infty \frac{{\rm d}\vartheta}{\vartheta}\xi_-(\vartheta) - 12\theta^2\int_\theta^\infty \frac{{\rm d}\vartheta}{\vartheta^3}\xi_-(\vartheta). \quad (5)$$

The E and B shear correlation functions are then given by

$$\xi_{\rm E}(\theta) = \frac{\xi_+(\theta)+\xi'(\theta)}{2}, \quad \xi_{\rm B}(\theta) = \frac{\xi_+(\theta)-\xi'(\theta)}{2}. \quad (6)$$

In the absence of systematics, $\xi_{\rm B} = 0$ and $\xi_{\rm E} = \xi_+$ (equation 3). In contrast with the $M_{\rm ap}$ statistics, the separation of the two modes depends on the signal integrated out with the scales probed by all surveys. One option is to calculate equation (6) using a fiducial cosmology to compute ξ_- on scales $\theta \rightarrow \infty$. As shown in Heymans et al. (2005), changes in the choice of fiducial cosmology do not significantly affect the results, allowing this statistic to be used as a diagnostic tool for the presence of systematics. This option does however prevent us from using $\xi_{\rm E}$ to constrain cosmology. As the statistical noise on the measured $\xi_{\rm E}$ is $\sim\sqrt{2}$ smaller than the statistical noise on the measured ξ_+, there is a more preferable alternative. If the survey size is sufficiently large in comparison to the scales probed by $\xi_{\rm E}$, we can consider the unknown integral to be a constant that can be calibrated using the aperture mass B-mode statistic $\langle M_{\rm ap}^2(\Delta\theta)\rangle_\perp$. A range $\Delta\theta$ of angular scales where $\langle M_{\rm ap}^2(\Delta\theta)\rangle_\perp \sim 0$ ensures that the B mode of the shear correlation function is zero as well (within the error bars), at angular scales $\sim\Delta\theta/5$. In this analysis we have calibrated $\xi_{\rm E,B}$ for our survey data in this manner. This alternative method has also been verified by recalculating $\xi_{\rm E,B}$ using our final best-fitting cosmology to extrapolate the signal. We find the two methods to be in very close agreement.

3 DATA DESCRIPTION

In this section we summarize the four weak-lensing surveys that form the 100-deg^2 weak-lensing survey: CFHTLS-Wide (Hoekstra et al. 2006), GaBoDs (Hetterscheidt et al. 2007), RCS (Hoekstra et al. 2002b) and VIRMOS-DESCART (Van Waerbeke et al. 2005), see Table 1 for an overview. Note that we have chosen not to include the CFHTLS-Deep data (Semboloni et al. 2006) in this analysis since the effective area of the analysed data is only 2.3 deg^2. Given the breadth of the parameter constraints obtained from this preliminary data set there is little value to be gained by combining it with four surveys which are among the largest available.

3.1 CFHTLS-Wide

The CFHTLS is a joint Canadian–French programme designed to take advantage of Megaprime, the CFHT wide-field imager. This 36 CCD mosaic camera has a 1×1-deg^2 field of view and a pixel scale of 0.187 arcsec per pixel. The CFHTLS has been allocated ∼450 nights over a 5 yr period (starting in 2003), the goal is to complete three independent survey components; deep, wide and very wide. The wide component will be imaged with five broad-band filters: u^*, g', r', i', z'. With the exception of u^* these filters are designed to match the Sloan Digital Sky Survey (SDSS) photometric system (Fukugita et al. 1996). The three wide fields will span a total of 170 deg^2 on completion. In this study, as in Hoekstra et al. (2006), we use data from the W1 and W3 fields that total 22 deg^2 after masking, and reach a depth of $i' = 24.5$. For detailed information concerning data reduction and object analysis the reader is referred to Hoekstra et al. (2006) and Van Waerbeke et al. (2002).

3.2 GaBoDS

The GaBoDS data set was obtained with the wide field imager (WFI) of the MPG/ESO 2.2-m telescope on La Silla, Chile. The camera consists of eight CCDs with a 34×33-arcmin^2 field of view and a pixel scale of 0.238 arcsec pixel^{-1}. The total data set consists of 52 statistically independent fields, with a total effective area (after trimming) of 13 deg^2. The magnitude limits of each field ranges between $R_{\rm VEGA} = 25.0$ and $R_{\rm VEGA} = 26.5$ (this corresponds to a 5σ detection in a 2-arcsec aperture). To obtain a homogeneous depth across the survey we follow Hetterscheidt et al. (2007) performing our lensing analysis with only those objects which lie in the complete magnitude interval $R \in [21.5, 24.5]$. For further details of the data set, and technical information regarding the reduction pipeline the reader is referred to Hetterscheidt et al. (2007).

3.3 VIRMOS-DESCART

The DESCART weak-lensing project is a theoretical and observational programme for cosmological weak-lensing investigations. The cosmic shear survey carried out by the DESCART team uses the CFH12k data jointly with the VIRMOS survey to produce a large homogeneous photometric sample in the *BVRI* broad-band filters. CFH12k is a 12 CCD mosaic camera mounted at the CFHT prime focus, with a 42×28-arcmin^2 field of view and a pixel scale

Table 1. Summary of the published results from each survey used in this study. The values for σ_8 correspond to $\Omega_{\rm m} = 0.24$, and are given for the Peacock & Dodds (1996) method of calculating the non-linear evolution of the matter power spectrum. The statistics listed were used in the previous analyses; the shear correlation functions $\xi_{\rm E,B}$ (equation 6), the aperture mass statistic $\langle M_{\rm ap}^2\rangle$ (equation (4)) and the top-hat shear variance $\langle\gamma_{\rm E,B}^2\rangle$ (see Van Waerbeke et al. 2005).

	CFHTLS-Wide	GaBoDS	RCS	VIRMOS-DESCART
Area (deg^2)	22.0	13.0	53	8.5
$N_{\rm fields}$	2	52	13	4
Magnitude range	$21.5 < i' < 24.5$	$21.5 < R < 24.5$	$22 < R_{\rm C} < 24$	$21 < I_{\rm AB} < 24.5$
$\langle z_{\rm source}\rangle$	0.81	0.78	0.6	0.92
$z_{\rm median}$	0.71	0.58	0.58	0.84
Previous analysis	Hoekstra et al. (2006)	Hetterscheidt et al. (2007)	Hoekstra et al. (2002b)	Van Waerbeke et al. (2005)
$\sigma_8(\Omega_{\rm m} = 0.24)$	0.99 ± 0.07	0.92 ± 0.13	0.98 ± 0.16	0.96 ± 0.08
Statistic	$\xi_{\rm E,B}(\theta)$	$\langle M_{ap}^2\rangle(\theta)$	$\langle M_{ap}^2\rangle(\theta)$	$\langle\gamma_{\rm E,B}^2\rangle(\theta)$

© 2007 The Authors. Journal compilation © 2007 RAS, MNRAS **381,** 702–712

of 0.206 arcsec pixel^{-1}. The VIRMOS-DESCART data consist of four uncorrelated patches of 2×2 deg^2 separated by more than 40°. Here, as in Van Waerbeke et al. (2005), we use I_{AB}-band data from all four fields, which have an effective area of 8.5 deg^2 after masking, and a limiting magnitude of $I_{AB} = 24.5$ (this corresponds to a 5σ detection in a 3-arcsec aperture). Technical details of the data set are given in Van Waerbeke et al. (2001) and McCracken et al. (2003), while an overview of the VIRMOS-DESCART survey is given in Le Fèvre et al. (2004).

3.4 RCS

The RCS is a galaxy cluster survey designed to provide a large sample of optically selected clusters of galaxies with redshifts between 0.3 and 1.4. The final survey covers 90 deg^2 in both R_C and z', spread over 22 widely separated patches of $\sim 2.1 \times 2.3$ deg^2. The northern half of the survey was observed using the CFH12k camera on the CFHT, and the southern half using the Mosaic II camera mounted at the Cerro Tololo Inter-American Observatory, Victor M. Blanco 4-m telescope prime focus. This camera has an eight CCD WFI with a 36×36-arcmin^2 field of view and a pixel scale of 0.27 arcsec pixel^{-1}. The data studied here, as in Hoekstra et al. (2002b), consist of a total effective area of 53 deg^2 of masked imaging data, spread over 13 patches, with a limiting magnitude of 25.2 (corresponding to a 5σ point source depth) in the R_C band. 43 deg^2 were taken with the CFHT, the remaining 10 deg^2 were taken with the Blanco telescope. A detailed description of the data reduction and object analysis is described in Hoekstra et al. (2002a), to which we refer for technical details.

4 COSMIC SHEAR SIGNAL

Lensing shear has been measured for each survey using the common KSB galaxy shape measurement method (Kaiser, Squires & Broadhurst 1995; Luppino & Kaiser 1997; Hoekstra et al. 1998). The practical application of this method to the four surveys differs slightly, as tested by STEP (Heymans et al. 2006a; Massey et al. 2007a), resulting in a small calibration bias in the measurement of the shear. Heymans et al. (2006a) define both a calibration bias (m) and an offset of the shear (c),

$$\gamma_{\rm meas} - \gamma_{\rm true} = m\gamma_{\rm true} + c, \tag{7}$$

where $\gamma_{\rm meas}$ is the measured shear, $\gamma_{\rm true}$ is the true shear signal, and m and c are determined from an analysis of simulated data. The value of c is highly dependent on the strength of the PSF distribution, therefore the value determined through comparisons with simulated data cannot be easily applied to real data whose PSF strength varies across the image. Since an offset in the shear will appear as residual B modes, we take $c = 0$, and focus on the more significant and otherwise unaccounted for shear bias (m). Equation (7) then simplifies to

$$\gamma_{\rm true} = \gamma_{\rm meas}(m + 1)^{-1}. \tag{8}$$

The calibration bias for the CFHTLS-Wide, RCS and VIRMOS-DESCART (HH analysis in Massey et al. (2007a)) is $m = -0.0017 \pm 0.0088$, and $m = 0.038 \pm 0.026$ for GaBoDS (MH analysis in Massey et al. (2007a)).

We measure the shear correlation functions $\xi_E(\theta)$ and $\xi_B(\theta)$ (equation 6) for each survey, shown in Fig. 1. As discussed in Section 2, these statistics are calibrated using the measured

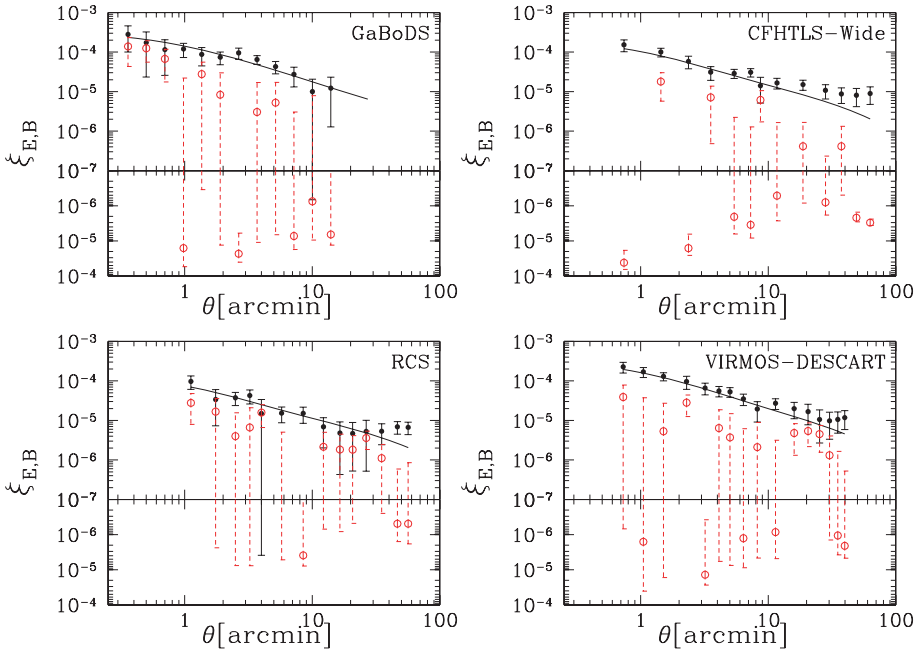

Figure 1. E and B modes of the shear correlation function ξ (filled and open points, respectively) as measured for each survey. Note that the 1σ errors on the E modes include statistical noise, non-Gaussian sample variance (see Section 6) and a systematic error given by the magnitude of the B mode. The 1σ error on the B modes is statistical only. The results are presented on a log–log scale, despite the existence of negative B modes. We have therefore collapsed the infinite space between 10^{-7} and zero, and plotted negative values on a separate log scale mirrored on 10^{-7}. Hence all values on the lower portion of the graph are negative, their absolute value is given by the scaling of the graph. Note that this choice of scaling exaggerates any discrepancies. The solid lines show the best-fitting ΛCDM model for $\Omega_m = 0.24$, $h = 0.72$, $\Gamma = h\Omega_m$, σ_8 given in Table 4, and $n(z)$ given in Table 2. The latter two being chosen for the case of the high-confidence redshift calibration sample, an $n(z)$ modelled by equation (10), and the non-linear power spectrum estimated by Smith et al. (2003).

© 2007 The Authors. Journal compilation © 2007 RAS, MNRAS **381,** 702–712

aperture-mass B-mode $\langle M_{\rm ap}^2\rangle_\perp$. The 1σ errors on $\xi_{\rm E}$ include statistical noise, computed as described in Schneider et al. (2002), non-Gaussian sample variance (see Section 6 for details), and a systematic error added in quadrature. The systematic error for each angular scale θ is given by the magnitude of $\xi_{\rm B}(\theta)$. The 1σ errors on $\xi_{\rm B}$ are statistical only. We correct for the calibration bias by scaling $\xi_{\rm E}$ by $(1+m)^{-2}$, the power of negative 2 arising from the fact that $\xi_{\rm E}$ is a second-order shear statistic. When estimating parameter constraints in Section 6.2 we marginalize over the error on the calibration bias, which expresses the range of admissible scalings of $\xi_{\rm E}$. Tables containing the measured correlation functions and their corresponding covariance matrices are included as supplementary material to the online version of this article.

5 REDSHIFT DISTRIBUTION

The measured weak-lensing signal depends on the redshift distribution of the sources, as seen from equation (1). Past weak-lensing studies (e.g. Massey et al. 2005; Van Waerbeke et al. 2005; Hoekstra et al. 2006; Semboloni et al. 2006) have used the *Hubble Deep Field* (HDF) photometric redshifts to estimate the shape of the redshift distribution. Spanning only 5.3 arcmin^2, the HDF suffers from sample variance as described in Van Waerbeke et al. (2006), where it is also suggested that the HDF fields may be subject to a selection bias. This sample variance of the measured redshift distribution adds an additional error to the weak-lensing analysis that is not typically accounted for.

In this study we use the largest deep photometric redshift catalogue in existence, from Ilbert et al. (2006), who have estimated redshifts on the four Deep fields of the T0003 CFHTLS release. The redshift catalogue is publicly available at terapix.iap.fr. The full photometric catalogue contains 522 286 objects, covering an effective area of 3.2 deg^2. A set of 3241 spectroscopic redshifts with $0 \leqslant z \leqslant 5$ from the VIRMOS VLT Deep Survey were used as a calibration and training set for the photometric redshifts. The resulting photometric redshifts have an accuracy of $\sigma_{(z_{\rm phot}-z_{\rm spec})/(1+z_{\rm spec})} = 0.043$ for $i'_{\rm AB} = 22.5-24$, with a fraction of catastrophic errors of 5.4 per cent. Ilbert et al. (2006) demonstrate that their derived redshifts work best in the range $0.2 \leqslant z \leqslant 1.5$, having a fraction of catastrophic errors of $\sim$5 per cent in this range. The fraction of catastrophic errors increases dramatically at $z < 0.2$ and $1.5 < z < 3$ reaching $\sim$40 and $\sim$70 per cent, respectively. This is explained by a degeneracy between galaxies at $z_{\rm spec} < 0.4$ and $1.5 < z_{\rm phot} < 3$ due to a mismatch between the Balmer break and the intergalactic Lyman α forest depression.

Van Waerbeke et al. (2006) estimate the expected sampling error on the average redshift for such a photometric redshift sample to be $\sim$3 per cent$/\sqrt{4} = 1.5$ per cent, where the factor of $\sqrt{4}$ comes from the four independent CFHTLS-Deep fields, a great improvement over the $\sim$10 per cent error expected for the HDF sample.

5.1 Magnitude conversions

In order to estimate the redshift distributions of the surveys, we calibrate the magnitude distribution of the photometric redshift sample (henceforth the $z_{\rm p}$ sample) to that of a given survey by converting the CFHTLS filter set $u^* g' r' i' z'$ to $I_{\rm AB}$ magnitudes for VIRMOS-DESCART and $R_{\rm VEGA}$ magnitudes for RCS and GaBoDS. We employ the linear relationships between different filter bands given by Blanton & Roweis (2007):

$$\begin{aligned} I_{\rm AB} &= i' - 0.0647 - 0.7177[(i'-z') - 0.2083], \\ R_{\rm VEGA} &= r' - 0.0576 - 0.3718[(r'-i') - 0.2589] - 0.21. \end{aligned} \quad (9)$$

These conversions were estimated by fitting spectral energy distribution templates to data from the SDSS. They are considered to be accurate to 0.05 mag or better, resulting in an error on our estimated median redshifts of at most 1 per cent, which is small compared to the total error budget on the estimated cosmological parameters.

5.2 Modelling the redshift distribution $n(z)$

The galaxy weights used in each survey's lensing analysis result in a weighted source redshift distribution. To estimate the effective $n(z)$ of each survey we draw galaxies at random from the $z_{\rm p}$ sample, using the method described in section 6.5.1 of Wall & Jenkins (2003) to reproduce the shape of the weighted magnitude distribution of each survey. A Monte Carlo (bootstrap) approach is taken to account for the errors in the photometric redshifts, as well as the statistical variations expected from drawing a random sample of galaxies from the $z_{\rm p}$ sample to create the redshift distribution. The process of randomly selecting galaxies from the $z_{\rm p}$ sample, and therefore estimating the redshift distribution of the survey, is repeated 1000 times. Each redshift that is selected is drawn from its probability distribution defined by the ±1 and $\pm3\sigma$ errors (since these are the error bounds given in the catalogue of Ilbert et al. (2006)). The sampling of each redshift is done such that a uniformly random value within the 1σ error is selected 68 per cent of the time, and a uniformly random value within the three sigma error (but exterior to the 1σ error) is selected 32 per cent of the time. The redshift distribution is then defined as the average of the 1000 constructions, and an average covariance matrix of the redshift bins is calculated.

At this point sample variance and Poisson noise are added to the diagonal elements of the covariance matrix, following Van Waerbeke et al. (2006). They provide a scaling relation between cosmic (sample) variance noise and Poisson noise where $\sigma_{\rm sample}/\sigma_{\rm Poisson}$ is given as a function of redshift for different-sized calibration samples. We take the curve for a 1-deg^2 survey, the size of a single CFHTLS-Deep field, and divide by $\sqrt{4}$ since there are four independent 1-deg^2 patches of sky in the photometric redshift sample.

Based on the photometric redshift sample of Ilbert et al. (2006) we consider two redshift ranges, the full range of redshifts in the photometric catalogues $0.0 \leqslant z \leqslant 4.0$, and the high-confidence range $0.2 \leqslant z \leqslant 1.5$. The goal is to assess to what extent this will affect the redshift distribution, and – in turn – the derived parameter constraints.

The shape of the normalized redshift distribution is often assumed to take the following form:

$$n(z) = \frac{\beta}{z_0\,\Gamma((1+\alpha)/\beta)} \left(\frac{z}{z_0}\right)^{\alpha} \exp\left[-\left(\frac{z}{z_0}\right)^{\beta}\right], \quad (10)$$

where α, β and z_0 are free parameters. If the full range of photometric redshifts is used the shape of the redshift distribution is poorly fitted by equation (10), this is a result of the function's exponential drop off which cannot accommodate the number of high-redshift galaxies in the tail of the distribution (see Fig. 2). We therefore adopt a new function in an attempt to better fit the normalized redshift distribution,

$$n(z) = N\frac{z^a}{z^b + c}, \quad (11)$$

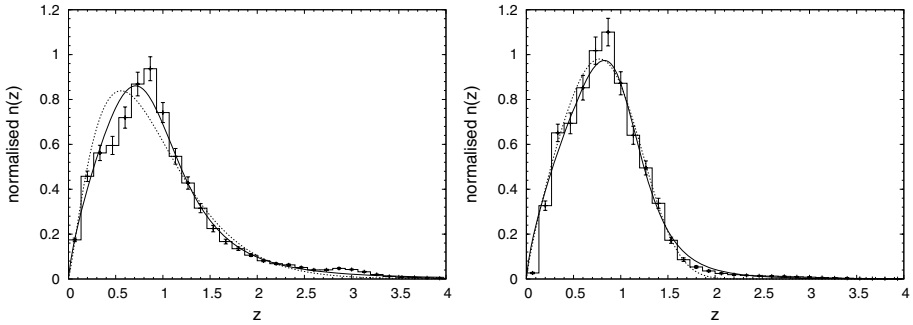

Figure 2. Normalized redshift distribution for the CFHTLS-Wide survey, given by the histogram, where the error bars include Poisson noise and sample variance of the photometric redshift sample. The dashed curve shows the best fit for equation (10), and the solid curve for equation (11). Left-hand panel: Distribution obtained if all photometric redshifts are used, that is, $0.0 \leqslant z \leqslant 4.0$, and χ^2 is calculated in the range $0.0 \leqslant z \leqslant 2.5$. Right-hand panel: Distribution obtained if only the high-confidence redshifts are used, that is, $0.2 \leqslant z \leqslant 1.5$, and χ^2 is calculated over this range. The existence of counts for $z > 1.5$ is a result of drawing the redshifts from their full probability distributions.

where a, b and c are free parameters, and N is a normalizing factor,

$$N = \left(\int_0^\infty \mathrm{d}z' \frac{z'^a}{z'^b + c} \right)^{-1}. \quad (12)$$

The best-fitting model is determined by minimizing the generalized χ^2 statistic:

$$\chi^2 = (d_i - m_i)\mathbf{C}^{-1}(d_i - m_i)^{\mathrm{T}}, \quad (13)$$

where $\mathbf{C}$ is the covariance matrix of the binned redshift distribution as determined from the 1000 Monte Carlo constructions, d_i is the number count of galaxies in the ith bin from the average of the 1000 distributions, and m_i is the number count of galaxies at the centre of the ith bin for a given model distribution. For each survey we determine the best fit for both equations (10) and (11). In either case we consider both the full range of redshifts and the high-confidence range, the results are presented in Table 2.

Fig. 2 shows the best-fitting models to the CFHTLS-Wide survey, when the full range of photometric redshifts is considered (left-hand panel), equation (11) clearly fits the distribution better than equation (10), having reduced χ^2 statistics of 2.41 and 8.94, respectively. When we consider only the high-confidence redshifts (right-hand panel of Fig. 2) both functions fit equally well having reduced χ^2 statistics of 1.65 and 1.63 for equation (11) and equation (10), respectively. Note that the redshift distribution as determined from the data (histograms in Fig. 2) is non-zero at $z > 1.5$ for the high-confidence photometric redshifts ($0.2 \leqslant z_{\mathrm{p}} \leqslant 1.5$) because of the Monte Carlo sampling of the redshifts from their probability distributions.

6 PARAMETER ESTIMATION

6.1 Maximum likelihood method

We investigate a 6D parameter space consisting of the mean matter density Ω_{m}, the normalization of the matter power spectrum σ_8, the Hubble parameter h and $n(z)$ the redshift distribution parametrized by either α, β and z_0 (equation 10) or a, b and c (equation 11). A flat cosmology ($\Omega_{\mathrm{m}} + \Omega_\Lambda = 1$) is assumed throughout, and the shape parameter is given by $\Gamma = \Omega_{\mathrm{m}}h$. The default priors are taken to be $\Omega_{\mathrm{m}} \in [0.1, 1]$, $\sigma_8 \in [0.5, 1.2]$ and $h \in [0.64, 0.8]$ with the latter in agreement with the findings of the *Hubble Space Telescope* key project (Freedman et al. 2001). The priors on the redshift distribution were arrived at using a Monte Carlo technique. This is necessary since the three parameters of either equation (10) or equation (11) are very degenerate, hence simply finding the 2 or 3σ levels of one parameter while keeping the other two fixed at their best-fitting values does not fairly represent the probability distribution of the redshift parameters. The method used ensures a sampling of parameter triplets whose number count follow the 3D probability distribution; that is 68 per cent lie within the 1σ volume, 97 per cent within the 2σ volume, etc. We find 100 such parameter trios and use them as the prior on the redshift distribution, therefore this is a Gaussian prior on $n(z)$.

Given the data vector $\boldsymbol{\xi}$, which is the shear correlation function (ξ_{E} of equation 6) as a function of scale, and the model prediction $\mathbf{m}$ (Ω_{m}, σ_8, h, $n(z)$) the likelihood function of the data is given by

$$\mathcal{L} = \frac{1}{\sqrt{(2\pi)^n |\mathbf{C}|}} \exp\left[-\frac{1}{2}(\boldsymbol{\xi} - \mathbf{m})\mathbf{C}^{-1}(\boldsymbol{\xi} - \mathbf{m})^{\mathrm{T}} \right], \quad (14)$$

Table 2. The best-fitting model parameters for the redshift distribution, given by either equation (10) or equation (11). Models are fitted using the full calibration sample of Ilbert et al. (2006) $0.0 \leqslant z_{\mathrm{p}} \leqslant 4.0$, and using only the high-confidence region $0.2 \leqslant z_{\mathrm{p}} \leqslant 1.5$. χ^2_ν is the reduced χ^2 statistic; $\langle z \rangle$ and z_{m} are the average and median redshift, respectively, calculated from the model on the range $0.0 \leqslant z \leqslant 4.0$.

		Equation (10)						Equation (11)						
		α	β	z_0	$\langle z \rangle$	z_{m}	χ^2_ν	a	b	c	N	$\langle z \rangle$	z_{m}	χ^2_ν
$0.2 \leqslant z_{\mathrm{p}} \leqslant 1.5$	CFHTLS-Wide	0.836	3.425	1.171	0.802	0.788	1.63	0.723	6.772	2.282	2.860	0.848	0.812	1.65
	GaBoDS	0.700	3.186	1.170	0.784	0.760	1.96	0.571	6.429	2.273	2.645	0.827	0.784	2.80
	RCS	0.787	3.436	1.157	0.781	0.764	1.41	0.674	6.800	2.095	2.642	0.823	0.788	1.60
	VIRMOS-DESCART	0.637	4.505	1.322	0.823	0.820	1.48	0.566	7.920	6.107	6.266	0.859	0.844	2.06
$0.0 \leqslant z_{\mathrm{p}} \leqslant 4.0$	CFHTLS-Wide	1.197	1.193	0.555	0.894	0.788	8.94	0.740	4.563	1.089	1.440	0.945	0.828	2.41
	GaBoDS	1.360	0.937	0.347	0.938	0.800	7.65	0.748	3.932	0.800	1.116	0.993	0.832	2.40
	RCS	1.423	1.032	0.391	0.888	0.772	5.67	0.819	4.418	0.800	1.201	0.939	0.808	1.84
	VIRMOS-DESCART	1.045	1.445	0.767	0.909	0.816	9.95	0.703	5.000	1.763	2.042	0.960	0.864	2.40

© 2007 The Authors. Journal compilation © 2007 RAS, MNRAS **381,** 702–712

Table 3. Data used for each survey to calculate the Gaussian contribution to the sample variance covariance matrix. $A_{\rm eff}$ is the effective area, $n_{\rm eff}$ the effective galaxy number density and $\sigma_{\rm e}$ the intrinsic ellipticity dispersion.

	$A_{\rm eff}$ (deg^2)	$n_{\rm eff}$ (arcmin^{-2})	$\sigma_{\rm e}$
CFHTLS-Wide	22	12	0.47
RCS	53	8	0.44
VIRMOS-DESCART	8.5	15	0.44
GaBoDS	13	12.5	0.50

where n is the number of angular scale bins and $\mathbf{C}$ is the $n \times n$ covariance matrix. The shear covariance matrix can be expressed as

$$C_{ij} = \langle (\xi_i - \mu_i)(\xi_j - \mu_j) \rangle, \tag{15}$$

where μ_i is the mean of the shear ξ_i at scale i, and angular brackets denote the average over many independent patches of sky. To obtain a reasonable estimate of the covariance matrix for a given set of data one needs many independent fields, this is not the case for either the CFHTLS-Wide or the VIRMOS-DESCART surveys.

We opt to take a consistent approach for all four data sets by decomposing the shear covariance matrix as $\mathbf{C} = \mathbf{C}_n + \mathbf{C}_{\rm B} + \mathbf{C}_{\rm s}$, where $\mathbf{C}_n$ is the statistical noise, $\mathbf{C}_{\rm B}$ is the absolute value of the residual B mode and $\mathbf{C}_{\rm s}$ is the sample variance covariance matrix. $\mathbf{C}_n$ can be measured directly from the data, it represents the statistical noise inherent in a finite data set. $\mathbf{C}_{\rm B}$ is diagonal and represents the addition of the B mode in quadrature to the uncertainty, this provides a conservative limit to how well the lensing signal can be determined.

For Gaussian sample variance the matrix $\mathbf{C}_{\rm s}$ can be computed according to Schneider et al. (2002), assuming an effective survey area $A_{\rm eff}$, an effective number density of galaxies $n_{\rm eff}$ and an intrinsic ellipticity dispersion $\sigma_{\rm e}$ (see Table 3). However, Schneider et al. (2002) assume Gaussian statistics for the fourth-order moment of the shear correlation function – a necessary simplification to achieve an analytic form for the sample variance covariance matrix. We use the calibration presented by Semboloni et al. (2007), estimated from ray-tracing simulations, to account for non-Gaussianities. Their work focuses on the following quantity:

$$\mathcal{F}(\vartheta_1, \vartheta_2) = \frac{\mathrm{C}_{\rm s}^{\rm meas}(\xi_+; \vartheta_1, \vartheta_2)}{\mathrm{C}_{\rm s}^{\rm Gaus}(\xi_+; \vartheta_1, \vartheta_2)}, \tag{16}$$

where $\mathcal{F}(\vartheta_1, \vartheta_2)$ is the ratio of the sample variance covariance measured from N-body simulations $[\mathrm{C}_{\rm s}^{\rm meas}(\xi_+; \vartheta_1, \vartheta_2)]$ to that expected from Gaussian effects alone $[\mathrm{C}_{\rm s}^{\rm Gaus}(\xi_+; \vartheta_1, \vartheta_2)]$. It is found that $\mathcal{F}(\vartheta_1, \vartheta_2)$ increases significantly above unity at scales smaller than $\sim$10 arcmin, increasing with decreasing scale, it reaches an order of magnitude by $\sim$2 arcmin. The parametrized fit as a function of mean source redshift is given by

$$\begin{aligned} \mathcal{F}(\vartheta_1, \vartheta_2) &= \frac{p_1(z)}{\left[\vartheta_1^2 \vartheta_2^2\right]^{p_2(z)}}, \\ p_1(z) &= \frac{16.9}{z^{0.95}} - 2.19, \\ p_2(z) &= 1.62\, z^{-0.68} \exp(-z^{-0.68}) - 0.03. \end{aligned} \tag{17}$$

A fiducial model is required to calculate the Gaussian covariance matrix, it is taken as $\Omega_{\rm m} = 0.3$, $\Lambda = 0.7$, $\sigma_8 = 0.8$, $h = 0.72$ and the best-fitting $n(z)$ model (see Table 2). We then use the above prescription to account for non-Gaussianities, increasing $\mathbf{C}_{\rm s}$ everywhere $\mathcal{F}$ is above unity. For each survey the total covariance matrix ($\mathbf{C} = \mathbf{C}_n + \mathbf{C}_{\rm s} + \mathbf{C}_{\rm B}$) is included as supplementary material to the online version of this article.

To test this method we compare our analytic covariance matrix for GaBoDS with that found by measuring it from the data (Hetterscheidt et al. 2007). Since GaBoDS images 52 independent fields it is possible to obtain an estimate of $\mathbf{C}$ directly from the data. The contribution from the B modes ($\mathbf{C}_{\rm B}$) is not added to our analytic estimate in this case, since its inclusion is meant as a conservative estimate of the systematic errors. We find a median per cent difference along the diagonal of $\sim$15 per cent, which agrees well with the accuracy obtained for simulated data (Semboloni et al. 2007).

6.2 Joint constraints on σ_8 and $\Omega_{\rm m}$

For the combined survey we place joint constraints on σ_8 and $\Omega_{\rm m}$ as shown in Fig. 3. Fitting to the maximum likelihood region we find $\sigma_8(\Omega_{\rm m}/0.24)^{0.59} = 0.84 \pm 0.05$, where the quoted error is 1σ for a hard prior of $\Omega_{\rm m} = 0.24$. This result assumes a flat Lambda cold dark matter (ΛCDM) cosmology and adopts the non-linear matter power spectrum of Smith et al. (2003). The redshift distribution is estimated from the high-confidence CFHTLS-Deep photometric redshifts using the standard $n(z)$ model given by equation (10). Marginalization was performed over $h \in [0.64, 0.80]$ with flat priors, $n(z)$ with Gaussian priors as described in Section 6.1, and a calibration bias of the shear signal with flat priors as discussed in Section 4. The corresponding constraints from each survey are presented in Fig. 4 and tabulated in Table 4. Results in Table 4 are presented for two methods of calculating the non-linear power spectrum; Peacock & Dodds (1996) and Smith et al. (2003). We find a difference of approximately 3 per cent in the best-fitting σ_8 values, where results using Smith et al. (2003) are consistently the smaller

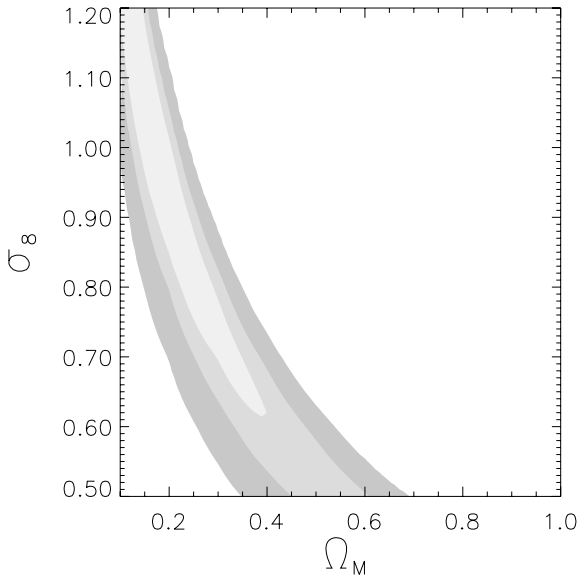

Figure 3. Joint constraints on σ_8 and $\Omega_{\rm m}$ from the 100-deg^2 weak-lensing survey assuming a flat ΛCDM cosmology and adopting the non-linear matter power spectrum of Smith et al. (2003). The redshift distribution is estimated from the high-confidence photometric redshift catalogue (Ilbert et al. 2006), and modelled with the standard functional form given by equation (10). The contours depict the 0.68, 0.95 and 0.99 per cent confidence levels. The models are marginalized, over $h = 0.72 \pm 0.08$, shear calibration bias (see Section 4) with uniform priors and the redshift distribution with Gaussian priors (see Section 6.1). Similar results are found for all other cases, as listed in Table 4.

© 2007 The Authors. Journal compilation © 2007 RAS, MNRAS **381,** 702–712

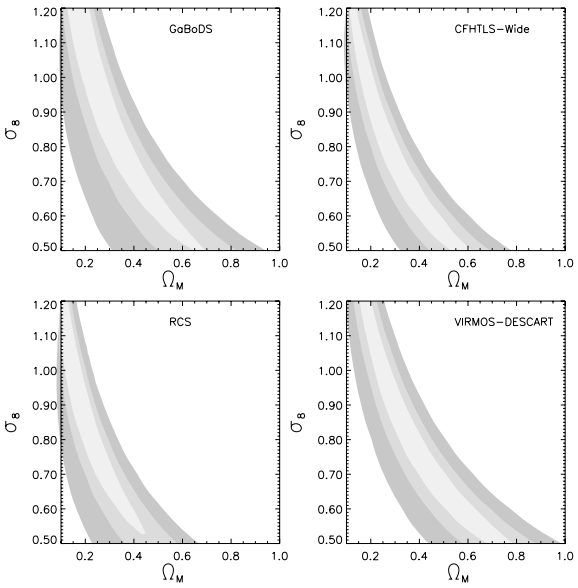

Figure 4. Joint constraints on σ_8 and Ω_m for each survey assuming a flat ΛCDM cosmology and adopting the non-linear matter power spectrum of Smith et al. (2003). The redshift distribution is estimated from the high-confidence photometric redshift catalogue (Ilbert et al. 2006), and modelled with the standard functional form given by equation (10). The contours depict the 0.68, 0.95 and 0.99 per cent confidence levels. The models are marginalized, over $h = 0.72 \pm 0.08$, shear calibration bias (see Section 4) with uniform priors, and the redshift distribution with Gaussian priors (see Section 6.1). Similar results are found for all other cases, as listed in Table 4.

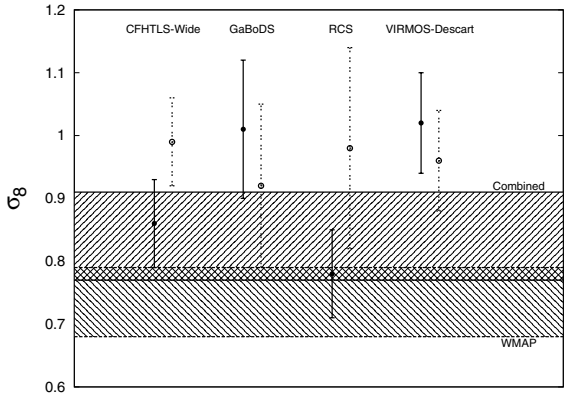

Figure 5. Values for σ_8 when Ω_m is taken to be 0.24, filled circles (solid) give our results with 1σ error bars, open circles (dashed) show the results from previous analyses (Table 1). Our results are given for the high-confidence photometric redshift catalogue, using the functional form for $n(z)$ given by equation (10), and the Smith et al. (2003) prescription for the non-linear power spectrum. The literature values use the Peacock & Dodds (1996) prescription for non-linear power, and are expected to be ∼3 per cent higher than would be the case for Smith et al. (2003). The forward slashed hashed region (enclosed by solid lines) shows the 1σ range allowed by our combined result, the back-slashed hashed region (enclosed by dashed lines) shows the 1σ range given by the *WMAP* 3-yr results.

of the two. The more recent results of Smith et al. (2003) are more accurate, and should be preferred over those of Peacock & Dodds (1996).

The contribution to the error budget due to the conservative addition of the B modes to the covariance matrix is small, amounting to at most 0.01 in the 1σ error bar for a hard prior of $\Omega_m = 0.24$. The analysis was also performed having removed all scales where the B modes are not consistent with zero (see Fig. 1). The resulting change in the best-fitting cosmology is small, shifting the best-fitting σ_8 for an Ω_m of 0.24 by at most 0.03 (for CFHTLS-Wide), and on average by ∼0.01 across all four surveys. These changes are well within our error budget.

We present a comparison of the measured σ_8 values with those previously published in Fig. 5. The quoted σ_8 values are for a vertical slice through $\sigma_8-\Omega_m$ space at an Ω_m of 0.24, and all error bars denote the 1σ region from the joint constraint contours. Our error bars (filled circles) are typically smaller than those from the literature (open circles) mainly due to the improved estimate of the redshift distribution. Our updated result for each survey agrees with the previous analysis within the error bars, this remains true if the literature values are lowered by ∼3 per cent to account for the difference in methods used for the non-linear power spectrum. Also plotted are the 1σ limits for the combined result and *Wilkinson Microwave Anisotropy Probe* (*WMAP*) 3-yr constraints (forward and back slashed hash regions, respectively), our result is consistent with *WMAP* at the 1σ level.

In addition to our main analysis we have investigated the impact of using four different models for the redshift distribution. These models are dependent on which functional form is used (equation 10 or 11) and which range is used for the photometric redshift sample ($0.0 \leqslant z_p \leqslant 4.0$ or $0.2 \leqslant z_p \leqslant 1.5$). Table 4 gives the best-fitting joint constraints on σ_8 and Ω_m, for each survey as well as the combined survey result.

Table 4. Joint constraints on the amplitude of the matter power spectrum σ_8, and the matter energy density Ω_m, parametrized as $\sigma_8(\Omega_m/0.24)^\alpha = \beta$. The errors are 1σ limits, calculated for a hard prior of $\Omega_m = 0.24$.

		$0.0 \leqslant z_p \leqslant 4.0$				$0.2 \leqslant z_p \leqslant 1.5$			
		Equation (10)		Equation (11)		Equation (10)		Equation (11)	
		β	α	β	α	β	α	β	α
Smith et al. (2003)	CFHTLS-Wide	0.84 ± 0.06	0.55	0.81 ± 0.07	0.54	0.86 ± 0.06	0.56	0.84 ± 0.06	0.55
	GaBoDS	0.93 ± 0.08	0.60	0.89 ± 0.09	0.59	1.01 ± 0.09	0.66	0.98 ± 0.10	0.63
	RCS	0.75 ± 0.07	0.55	0.73 ± 0.08	0.55	0.78 ± 0.07	0.57	0.76 ± 0.07	0.56
	VIRMOS-DESCART	0.99 ± 0.08	0.59	0.95 ± 0.07	0.58	1.02 ± 0.07	0.60	1.00 ± 0.08	0.59
	Combined	0.80 ± 0.05	0.57	0.77 ± 0.05	0.56	0.84 ± 0.05	0.59	0.82 ± 0.06	0.58
Peacock & Dodds (1996)	CFHTLS-Wide	0.87 ± 0.07	0.57	0.83 ± 0.06	0.56	0.89 ± 0.06	0.58	0.87 ± 0.06	0.57
	GaBoDS	0.96 ± 0.09	0.62	0.93 ± 0.08	0.60	1.04 ± 0.09	0.66	1.01 ± 0.09	0.64
	RCS	0.77 ± 0.07	0.57	0.74 ± 0.07	0.56	0.81 ± 0.08	0.58	0.79 ± 0.08	0.58
	VIRMOS-DESCART	1.02 ± 0.07	0.60	0.98 ± 0.07	0.59	1.05 ± 0.07	0.62	1.03 ± 0.08	0.61
	Combined	0.82 ± 0.05	0.58	0.79 ± 0.05	0.57	0.86 ± 0.06	0.60	0.84 ± 0.06	0.59

© 2007 The Authors. Journal compilation © 2007 RAS, MNRAS **381,** 702–712

Comparing the best-fitting σ_8 values with the average redshifts listed in Table 2, we find, as expected, that higher redshift models result in lower values for σ_8. Attempting to quantify this relation in terms of mean redshift fails. Changes in mean redshift are large (∼14 per cent) between the photometric samples, compared to ∼6 per cent between the two $n(z)$ models; however, a ∼5 per cent change in σ_8 is seen for both. The median redshift is a much better gauge, changing by ∼4 per cent between both photometric samples and $n(z)$ models. Precision cosmology at the 1 per cent level will necessitate roughly the same level of precision of the median redshift. Future cosmic shear surveys will require thorough knowledge of the complete redshift distribution of the sources, in particular to what extent a high-redshift tail exists.

7 DISCUSSION AND CONCLUSION

We have performed an analysis of the 100-deg^2 weak-lensing survey that combines four of the largest weak-lensing data sets in existence. Our results provide the tightest weak-lensing constraints on the amplitude of the matter power spectrum σ_8 and matter density Ω_m and a marked improvement on accuracy compared to previous results. Using the non-linear prediction of the cosmological power spectra given in Smith et al. (2003), the high-confidence region of the photometric redshift calibration sample, and equation (10) to model the redshift distribution, we find $\sigma_8(\frac{\Omega_m}{0.24})^{0.59} = 0.84 \pm 0.05$ for a hard prior of $\Omega_m = 0.24$.

Our analysis differs from previous weak-lensing analyses in three important aspects. We correctly account for non-Gaussian sample variance using the method of Semboloni et al. (2007), thus improving upon the purely Gaussian contribution given by Schneider et al. (2002). Using the results from STEP (Massey et al. 2007a) we correct for the shear calibration bias and marginalize over our uncertainty in this correction. In addition we use the largest deep photometric redshift catalogue in existence (Ilbert et al. 2006) to provide accurate models for the redshift distribution of sources; we also account for the effects of sample variance in these distributions (Van Waerbeke et al. 2006).

Accounting for the non-Gaussian contribution to the shear covariance matrix, which dominates on small scales, is very important. The non-Gaussian contribution is about twice that of the Gaussian contribution alone at a scale of 10 arcmin, this discrepancy increases to about an order of magnitude at 2 arcmin. This increases the errors on the shear correlation function at small scales, leading to slightly weaker constraints on cosmology. Ideally we would estimate the shear covariance directly from the data, as is done in the previous analyses for both GaBoDS (Hetterscheidt et al. 2007) and RCS (Hoekstra et al. 2002b). However, since we cannot accomplish this for all the surveys in this work, due to a deficit of independent fields, we opt for a consistent approach by using the analytic treatment along with the non-Gaussian calibration as described in Semboloni et al. (2007).

Accurate determination of the redshift distribution of the sources is crucial for weak-lensing cosmology since it is strongly degenerate with cosmological parameters. Past studies using small external photometric catalogues (such as the HDF) suffered from sample variance, a previously unquantified source of error that is taken into account here using the prescription of Van Waerbeke et al. (2006). In most cases the revised redshift distributions were in reasonable agreement with previous results; however, this was not the case for the RCS survey. We found that the previous estimation was biased toward low redshift (see Fig. 6), resulting in a significantly larger estimation of $\sigma_8(0.86^{+0.04}_{-0.05}$ for $\Omega_m = 0.3)$ than is presented here

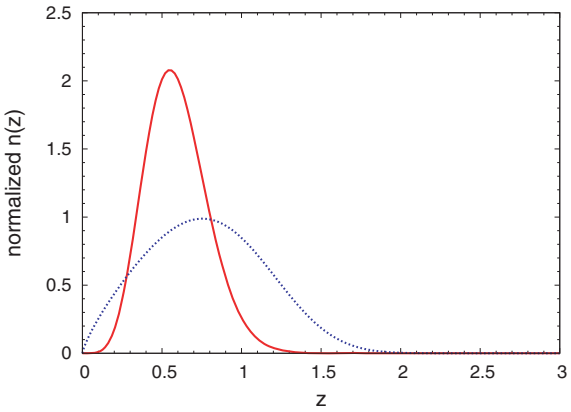

Figure 6. Redshift distributions for the RCS survey. The solid line shows the best-fitting $n(z)$ from Hoekstra et al. (2002b), the dashed curve is our best-fitting $n(z)$, the average redshifts are 0.6 and 0.78, respectively.

(0.69 ± 0.07). This difference is primarily due to a problem in the filter set conversion, between those used to image HDF (*F300W*, *F450W*, *F606W* and *F814W*) and the Cousins R_C filter used by RCS. The less severe changes in σ_8 for the other surveys, shown in Fig. 5, can also be largely understood from the updated redshift distributions. Comparing the median redshifts from the previous results (Table 1) to those presented here (Table 2) there exists a clear trend associating increases in median redshift to decreases in estimated σ_8 (see Fig. 5) and vice versa. Our estimate of median redshift for CFHTLS-Wide increases by ∼10 per cent and a corresponding decrease in σ_8 is seen, a similar correspondence is seen for VIRMOS-DESCART where the decreased median redshift in this analysis results in a proportionately larger value of σ_8. The change in σ_8 for GaBoDS, however, cannot be understood by comparing median redshifts since the previous results use a piece wise function to fit the redshift distribution, hence comparing median redshifts is not meaningful.

Our revised cosmological constraints introduce tension, at the $\sim 2\sigma$ level, between the results from the VIRMOS-DESCART and RCS survey as shown in Fig. 5. In this analysis we have accounted for systematic errors associated with shear measurement but have neglected potential systematics arising from correlations between galaxy shape and the underlying density field. This is valid in the case of intrinsic galaxy alignments which are expected to contribute less than a per cent of the cosmic shear signal for the deep surveys used in this analysis (Heymans et al. 2006b). What is currently uncertain however is the level of systematic error that arises from shear–ellipticity correlations (Hirata & Seljak 2004; Mandelbaum et al. 2006; Heymans et al. 2006b; Hirata et al. 2007) which could reduce the amplitude of the measured shear correlation function by ∼10 per cent (Heymans et al. 2006b). It has been found from the analysis of the SDSS (Mandelbaum et al. 2006; Hirata et al. 2007) that different morphological galaxy types contribute differently to this effect. It is therefore possible that the different *R*-band imaging of the RCS and the slightly lower median survey redshift make it more susceptible to this type of systematic error. Without complete redshift information for each survey, however, it is not possible to test this hypothesis or to correct for this potential source of error. In the future deep multicolour data will permit further investigation and correction for this potential source of systematic error.

In addition to using the best available photometric redshifts, we marginalize over the redshift distribution by selecting parameter triplets from their full 3D probability distribution, instead of fixing

two parameters and varying the third as is often done. Thus the marginalization is representative of the full range of $n(z)$ shapes, which are difficult to probe by varying one parameter due to degeneracies.

We have conducted our analysis using two different functional forms for the redshift distribution, the standard form given in equation (10) and a new form given by equation (11). The new function is motivated by the presence of a high-z tail when the entire photometric catalogue ($0.0 \leqslant z_p \leqslant 4.0$) is used to estimate the redshift distribution, equation (10) does a poor job of fitting this distribution (Fig. 2). However, when we restrict the photometric catalogue to the high-confidence region ($0.2 \leqslant z_p \leqslant 1.5$) both functions fit well, and the tendency for equation (11) to exhibit a tail towards high-z increases the median redshift resulting in a slightly lower estimate of σ_8. Though the tail of the distribution has only a small fraction of the total galaxies, they may have a significant lensing signal owing to their large redshifts. The influences of the different redshift distributions on cosmology is consistent within our 1σ errors but as survey sizes grow and statistical noise decreases, such differences will become significant. As the CFHTLS-Deep will be the largest deep photometric redshift catalogue for some years to come, this possesses a serious challenge to future surveys attempting to do precision cosmology. To assess the extent of any high-redshift tail, future surveys should strive to include photometric bands in the near-infrared, allowing for accurate redshift estimations beyond $z = 1.5$.

For $\Omega_m = 0.24$, the combined results using equation (10) are 0.80 ± 0.05 and 0.84 ± 0.05 for the unrestricted and high-confidence photometric redshifts, respectively, using equation (11) we find 0.77 ± 0.05 and 0.82 ± 0.06 (these results use the non-linear power spectrum given by Smith et al. (2003)). For completeness we provide results for both the Smith et al. (2003) and Peacock & Dodds (1996) non-linear power spectra, the resulting σ_8 values differ by $\sim$3 per cent of the Smith et al. (2003) value which is consistently the smaller of the two. The Smith et al. (2003) study is known to provide a more accurate estimation of the non-linear power than that of Peacock & Dodds (1996), for this reason we prefer the results obtained using the Smith et al. (2003) model. However, given the magnitude of variations resulting from different redshift distributions, this difference is not an important issue in the current work. Accurately determining the non-linear matter power spectrum is another challenge for future lensing surveys intent on precision cosmology. Alternatively, surveys focusing only on the large-scale measurement of the shear (Fu et al. 2007) are able to avoid complications arising from the estimation of non-linear power on small scales.

Surveys of varying depth provide different joint constraints in the $\Omega_m - \sigma_8$ plane, thus combining their likelihoods produces some degeneracy breaking. Taking the preferred prescription for the non-linear power spectrum, and using equation (10) along with the high-confidence photometric redshifts to estimate the redshift distribution, we find an upper limit of $\Omega_m < \sim 0.4$ and a lower limit of $\sigma_8 > \sim 0.6$ both at the 1σ level (see Fig. 3).

Weak lensing by a large-scale structure is an excellent means of constraining cosmology. The unambiguous interpretation of the shear signal allows for a direct measure of the dark matter power spectrum, allowing for a unique and powerful means of constraining cosmology. Our analysis has shown that accurately describing the redshift distribution of the sources is vital to future surveys intent on precision cosmology. Including near-infrared bands to photometric redshift estimates will be a crucial step in achieving this goal, allowing for reliable redshift estimates at $z > 1.5$ and assessing the extent of a high-z tail.

ACKNOWLEDGMENTS

We would like to thank to the referee for very prompt and useful comments. JB is supported by the Natural Sciences and Engineering Research Council (NSERC), and the Canadian Institute for Advanced Research (CIAR). CH acknowledges the support of the European Commission Programme 6th frame work, Marie Curie Outgoing International Fellowship, contract number M01F-CT-2006-21891, and a CITA National Fellowship. ES thanks the hospitality of the University of British Columbia, which made this collaboration possible. LVW and HH are supported by NSERC, CIAR and the Canadian Foundation for Innovation (CFI). YM thanks the Alexander Humboldt Foundation and the Terapix data centre for support, and the AIfA for hospitality. This work is partly based on observations obtained with MegaPrime equipped with MegaCam, a joint project of CFHT and CEA/DAPNIA, at the CFHT which is operated by the National Research Council (NRC) of Canada, the Institut National des Science de l'Univers of the Centre National de la Recherche Scientifique (CNRS) of France, and the University of Hawaii. This work is based in part on data products produced at TERAPIX and the Canadian Astronomy Data Centre as part of the CFHTLS, a collaborative project of NRC and CNRS. This research was performed with infrastructure funded by the Canadian Foundation for Innovation and the British Columbia Knowledge Development Fund (A Parallel Computer for Compact-Object Physics). This research has been enabled by the use of WestGrid computing resources, which are funded in part by the Canada Foundation for Innovation, Alberta Innovation and Science, BC Advanced Education, the participating research institutions. WestGrid equipment is provided by IBM, Hewlett Packard and SGI. This paper makes use of photometric redshifts produced jointly by Terapix and VVDS teams.

REFERENCES

Astier P. et al., 2006, A&A, 447, 31
Bacon D. J., Refregier A. R., Ellis R. S., 2000, MNRAS, 318, 625
Bacon D. J., Massey R. J., Refregier A. R., Ellis R. S., 2003, MNRAS, 344, 673
Bacon D. J. et al., 2005, MNRAS, 363, 723
Bartelmann M., Schneider P., 2001, Phys. Rep., 340, 291
Blanton M. R., Roweis S., 2007, AJ, 133, 734
Brown M. L., Taylor A. N., Bacon D. J., Gray M. E., Dye S., Meisenheimer K., Wolf C., 2003, MNRAS, 341, 100
Crittenden R. G., Natarajan P., Pen U.-L., Theuns T., 2001, ApJ, 559, 552
Crittenden R. G., Natarajan P., Pen U.-L., Theuns T., 2002, ApJ, 568, 20
Freedman W. L. et al., 2001, ApJ, 553, 47
Fu L. et al., 2007, MNRAS, submitted
Fukugita M., Ichikawa T., Gunn J. E., Doi M., Shimasaku K., Schneider D. P., 1996, AJ, 111, 1748
Hamana T. et al., 2003, ApJ, 597, 98
Hetterscheidt M., Simon P., Schirmer M., Hildebrandt H., Schrabback T., Erben T., Schneider P., 2007, A&A, 468, 859
Heymans C. et al., 2005, A&A, 361, 160
Heymans C. et al., 2006a, MNRAS, 368, 1323
Heymans C., White M., Heavens A., Vale C., Van Waerbeke L., 2006b, MNRAS, 371, 750
Hirata C. M., Seljak U., 2004, Phys. Rev. D, 70, 063526
Hirata C. M., Mandelbaum R., Ishak M., Seljak U., Nichol R., Pimbblet K. A., Ross N. P., Wake D., 2007, MNRAS, in press doi:10.1111/j.1365-2966.2007.12312.x (astro-ph/0701671)
Hoekstra H., Franx M., Kuijken K., Squires G., 1998, ApJ, 504, 636
Hoekstra H., Yee H. K. C., Gladders M. D., Barrientos L. F., Hall P. B., Infante L., 2002a, ApJ, 572, 55
Hoekstra H., Yee H. K. C., Gladders M. D., 2002b, ApJ, 577, 595

Hoekstra H. et al., 2006, ApJ, 647, 116
Ilbert O. et al., 2006, A&A, 457, 841
Jarvis M., Bernstein G. M., Fischer P., Smith D., Jain B., Tyson J. A., Wittman D., 2003, AJ, 125, 1014
Jarvis M., Jain B., Bernstein G., Dolney D., 2006, ApJ, 644, 71
Kaiser N., Squires G., Broadhurst T., 1995, ApJ, 449, 460
Kaiser N., Wilson G., Luppino G. A., 2000, ApJL, submitted (astro-ph/0003338)
Kitching T. D., Heavens A. F., Taylor A. N., Brown M. L., Meisenheimer K., Wolf C., Gray M. E., Bacon D. J., 2007, MNRAS, 376, 771
Le Fèvre O. et al., 2004, A&A, 417, 839
Luppino G. A., Kaiser N., 1997, ApJ, 475, 20
Mandelbaum R., Hirata C. M., Ishak M., Seljak U., Brinkmann J., 2006, MNRAS, 367, 611
Massey R., Refregier A., Bacon D. J., Ellis R., Brown M. L., 2005, MNRAS, 359, 1277
Massey R. et al., 2007a, MNRAS, 376, 13
Massey R. et al., 2007b, ApJL, in press (astro-ph/0701480)
McCracken H. J. et al., 2003, A&A, 410, 17
Munshi D., Valageas P., Van Waerbeke L., Heavens A., 2006, Phys. Rev., submitted (astro-ph/0612667)
Peacock J. A., Dodds S. J., 1996, MNRAS, 280, L19
Pen U.-L., Van Waerbeke L., Mellier Y., 2002, ApJ, 567, 31
Rhodes J., Refregier A., Collins N. R., Gardner J. P., Groth E. J., Hill R. S., 2004, ApJ, 605, 29
Schimd C. et al., 2007, A&A, 463, 405
Schneider P., Van Waerbeke L., Jain B., Kruse G., 1998, MNRAS, 296, 873
Schneider P., Van Waerbeke L., Kilbinger M., Mellier Y., 2002, A&A, 396, 1
Schrabback T. et al., 2007, A&A, 468, 823
Semboloni E. et al., 2006, A&A, 452, 51
Semboloni E., Van Waerbeke L., Heymans C., Hamana T., Colombi S., White M., Mellier Y., 2007, MNRAS, 375, L6
Smith R. E. et al., 2003, MNRAS, 341, 1311
Spergel D. N. et al., 2007, ApJL, 170, 377
Van Waerbeke L. et al., 2000, A&A, 358, 30
Van Waerbeke L. et al., 2001, A&A, 374, 757
Van Waerbeke L., Mellier Y., Pelló R., Pen U.-L., McCracken H. J., Jain B., 2002, A&A, 393, 369
Van Waerbeke L., Mellier Y., Hoekstra H., 2005, A&A, 429, 75
Van Waerbeke L., White M., Hoekstra H., Heymans C., 2006, Astropart. Phys., 26, 91
Wall J. V., Jenkins C. R., 2003, in Ellis R., Huchra J., Kahn S., Rieke G., Stetson P. B., eds, Princeton Series in Astrophysics: Practical Statistics for Astronomers. Cambridge Univ. Press, Cambridge
Wittman D., 2005, ApJ, 632, L5
Wittman D. M., Tyson J. A., Kirkman D., Dell'Antonio I., Bernstein G., 2000, Nat, 405, 143

APPENDIX A: SHEAR CORRELATION FUNCTION AND COVARIANCE MATRIX FOR THE SURVEYS

We present both the measured shear correlation function and the covariance matrix for each survey. The shear correlation function, given in Tables S1, S2, S3 and S4 for the CFHTLS-Wide, GaBoDS, RCS and VIRMOS-DESCART surveys, respectively, has been calibrated on large scales where $\langle M_{\rm ap}^2(\Delta\theta)\rangle_\perp$ is consistent with zero as described in Section 4.

Tables S5, S6, S7 and S8 for the CFHTLS-Wide, GaBoDS, RCS and VIRMOS-DESCART surveys, respectively, tabulate the correlation coefficient matrix:

$$\mathbf{r}_{ij} = \frac{\mathbf{C}_{ij}}{\left\langle \xi_i^2 \right\rangle^{1/2} \left\langle \xi_j^2 \right\rangle^{1/2}}, \tag{A1}$$

where $\mathbf{C}$ is the covariance matrix for each survey, as described in Section 6. We also tabulate $\langle \xi_i^2 \rangle$ so that the covariance matrix may be calculated from the correlation coefficient matrix. Note that $\langle \xi_i^2 \rangle$ is the variance of the i^{th} scale, equivalent to $\mathbf{C}_{ii}$.

Tables S1–S8 are available as supplementary material to the online version of this article.

SUPPLEMENTARY MATERIAL

The following supplementary material is available for this article:

Table S1. The columns are scale in arcminutes, E and B modes of the shear correlation function for the CFHTLS-Wide survey and finally the statistical contribution to the error given as the standard deviation.

Table S2. The columns are scale in arcminutes, E and B modes of the shear correlation function for GaBoDS and finally the statistical contribution to the error given as the standard deviation.

Table S3. The columns are scale in arcminutes, E and B modes of the shear correlation function for the RCS and finally the statistical contribution to the error given as the standard deviation.

Table S4. The columns are scale in arcminutes, E and B modes of the shear correlation function for VIRMOS-DESCART and finally the statistical contribution to the error given as the standard deviation.

Table S5. The first column is $\langle \xi_i^2 \rangle$ given in units of 10^{-10}, and can be used to reconstruct the covariance matrix $\mathbf{C}$. The remaining columns give the correlation coefficient matrix ($\mathbf{r}$) for the CFHTLS-Wide survey, which is an $n \times n$ matrix, where the n scales are given in the first column of Table S1. Small to large scales are arranged in ascending order from the top left-hand corner to the bottom right-hand corner of the matrix.

Table S6. The first column is $\langle \xi_i^2 \rangle$ given in units of 10^{-10}, and can be used to reconstruct the covariance matrix $\mathbf{C}$. The remaining columns give the correlation coefficient matrix ($\mathbf{r}$) for the GaBoDS survey, which is an $n \times n$ matrix, where the n scales are given in the first column of Table S2. Small to large scales are arranged in ascending order from the top left-hand corner to the bottom right-hand corner of the matrix.

Table S7. The first column is $\langle \xi_i^2 \rangle$ given in units of 10^{-10}, and can be used to reconstruct the covariance matrix $\mathbf{C}$. The remaining columns give the correlation coefficient matrix ($\mathbf{r}$) for the RCS survey, which is an $n \times n$ matrix, where the n scales are given in the first column of Table S3. Small to large scales are arranged in ascending order from the top left-hand corner to the bottom right-hand corner of the matrix.

Table S8. The first column is $\langle \xi_i^2 \rangle$ given in units of 10^{-10}, and can be used to reconstruct the covariance matrix $\mathbf{C}$. The remaining columns give the correlation coefficient matrix ($\mathbf{r}$) for the VIRMOS-DESCART survey, which is an $n \times n$ matrix, where the n scales are given in the first column of Table S4. Small to large scales are arranged in ascending order from the top left-hand corner to the bottom right-hand corner of the matrix.

This material is available as part of the online paper from: http://www.blackwell-synergy.com/doi/abs/10.1111/j.1365-2966.2007.12202.x
(this link will take you to the article abstract).

Please note: Blackwell Publishing are not responsible for the content or functionality of any supplementary materials supplied by the authors. Any queries (other than missing material) should be directed to the corresponding author for the article.

This paper has been typeset from a TEX/LATEX file prepared by the author.